Chapter 3
MATERIALS, STRUCTURES, AND FABRICATION

In the past, bismuth has been the material of choice for microbolometers because of its favorable temperature coefficient of resistivity, and because of its thin film resistivity, which allows easy impedance-matching to planar antennas. In this chapter, some of the properties of Bi will be investigated, and another material, tellurium, will also be examined for use as a microbolometer. Device fabrication will be detailed, including a discussion of a bilayer photoresist bridge technique. The high resistivity of Te prevents simple impedance-matching to a planar antenna, so a composite structure which overcomes this mismatch problem is discussed. The chapter culminates in the fabrication and performance details of a Te composite microbolometer.

3.1 Bismuth

Bismuth (Bi) occurs as a light grey metal with a melting point at 271 °C. It has the lowest thermal conductivity of any metal except mercury, and is often used as a thermocouple material because of its high thermal emf. The crystal structure is rhombohedral with a 2-atom basis (see for instance [1]). This can be visualized by starting with a cubic cell (Fig. 3.1a), and pulling on one corner in the (111) direction to distort the cell (Fig. 3.1b). Then, the dark atoms in Fig. 3.1b are moved slightly in the (111) direction to give the structure shown in Fig. 3.1c. The atoms in a layer are held fairly tightly together, but atoms in adjacent layers are held together only by weak London forces. This accounts for the fragility of Bi films.

Thin films of bismuth show a polycrystalline columnular structure, with grain sizes on the order of the film thickness. The texture of the film depends strongly on the substrate, but the crystals are preferentially oriented with the trigonal axis (111) of the rhombohedral crystal perpendicular to the substrate [2-34]. These films are most generally prepared by thermal evaporation in a vacuum under 10^{-5} torr at a

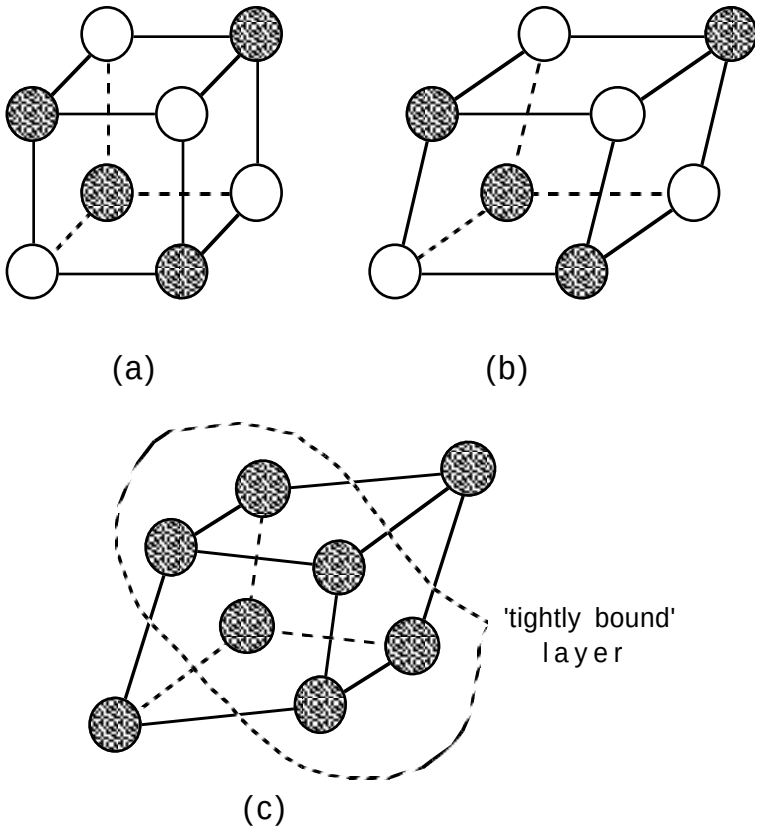

Fig. 3.1: The rhombohedral crystal structure can be visualized by starting with a cubic cell, as in (a), with every other Bi atom shaded. In (b), the cell is stretched in the (111) direction. Finally, the dark atoms from (b) are moved slightly in the (111) direction to give the structure shown in (c), where now all Bi atoms are shaded.

deposition rate of between 1 and 20 Å/sec. The most common substrate for Bi deposition discussed in the literature is glass, and deposition temperatures range from 20°C to 150°C. Table 3.1 shows some of the properties of thin film Bi taken from a number of references. From this table, it is apparent that the properties of thin film Bi are quite variable.

Kawazu *et al.* demonstrated that the largest grain sizes are produced using high substrate temperature and a slow deposition rate [5]. As temperature is raised to 200°C, however, the Bi does not stick well to the substrate, resulting in very rough films. For films about 1000 Å thick, the substrate temperature could be

Reference	Substrate type and temp.	Deposition rate (Å/sec)	film thickness (Å)	Resistivity at 300 K μΩ-cm
Joglekar [6]	glass 25°C	2	1000	1000
Baba [3]	muscovite 100°C	1	300 3350	850 160
Kawazu [5]	(111) Si 100°C	5	2000 5000	200 160
Chaudhuri [7]	glass 150°C	2-3	900 2600	470 240
Kochowski [2]	glass 20°C	5-15	200 3000	600 280
Vandamme [8]	glass 60°C	20	300 14000	800 200
Kuijper [9]	glass 60°C	20	1300 27000	800 350
Völklein [4]	400 Å thick cellulose acetate foil 25°C	10	280 1060 3500	690 455 360
Neikirk [10]	glass 25°C	1-5	1000	685
Wentworth [11]	glass	5-10	1000	910

Table 3.1: Comparison of selected unannealed thin film bismuth data from a number of references.

increased to up to 140°C at a 1 Å/sec deposition rate to produce the largest crystals.

What makes thin film Bi interesting is its peculiar resistivity behavior as a function of temperature. In Fig. 3.2 (adapted from [3]), resistivity ρ is plotted as a function of temperature T for several film thicknesses. First, this plot shows that thin films of Bi have a higher resistivity than bulk Bi. The higher resistivity is a result of increased scattering at the more numerous grain boundaries for thin films. There is also a region of decreasing resistance for increasing temperature. This behavior is similar to that of a semiconductor, which has a decreasing resistance caused by the excitation of more carriers as the temperature rises. However, at

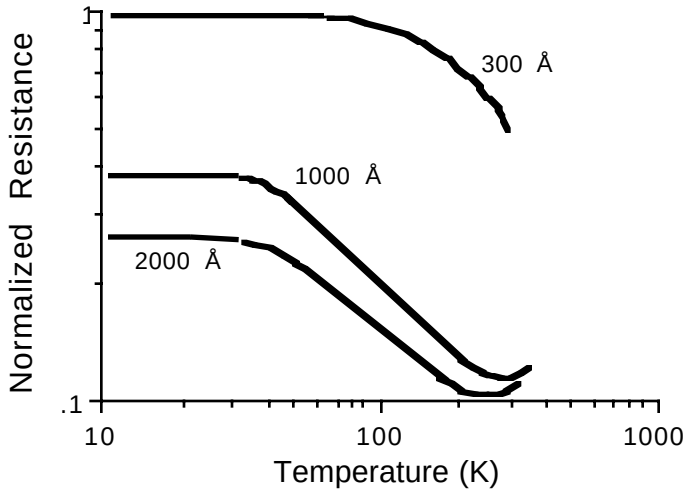

Fig. 3.2: Resistivity vs temperature for several thicknesses of Bi. The resistance is normalized to the resistance of the 300 Å thick film. These plots are adapted from data by Baba *et al* . [3].

higher temperatures, the Bi acts like a metal: the resistivity increases as temperature increases because there are more lattice vibrations acting to reduce carrier mobility.

The negative resistivity is a consequence of two competing mechanisms [3,8[12]]. First, the carrier concentration increases with increasing T, as shown in Fig. 3.3a. Second, the carrier mobility decreases with increasing temperature, as shown in Fig. 3.3b. Figure 3.3c shows the resulting conductivity, which is proportional to the product of μ and n. The region of positive $d\sigma/dT$ corresponds to the negative temperature coefficient of resistivity. Notice that for low temperatures, the mobility changes very slowly. This is because mobility is proportional to the mean-free-path (mfp) of the charge carrier, and this mfp can be no bigger than the crystalline size. Thus, as the temperature falls, the mobility can only increase to the point where it becomes limited by the crystallite size, and the region of negative α shifts to higher temperatures as the film thickness decreases [3].

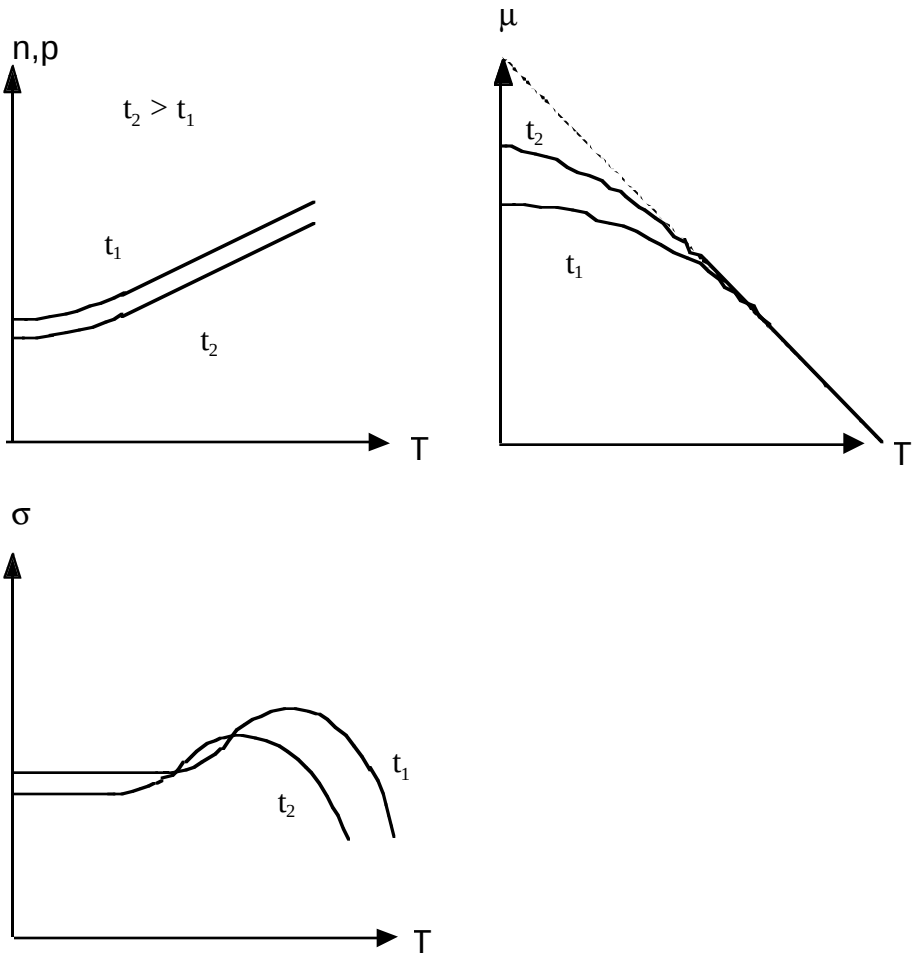

Fig. 3.3: The behavior of Bi thin films, as a function of thickness t_1 and t_2, and of temperature. (a) Carrier concentration increases with temperature. (b) Mobility decreases with temperature, but for low temperature, mobility is limited by the mean-free-path of the crystal. (c) The product of the carrier concentration and mobility is proportional to the conductivity, and the positive sloped region for σ corresponds to a negative temperature coefficient of resistivity. These plots are adapted from Baba *et al.* [3].

3.2 Tellurium

Thin films of tellurium have been the focus of a number of investigations for sensor-type applications [13-1415]. This is a rather simple element to evaporate, since it sublimes at a relatively low temperature (277 °C). Te will oxidize to some extent in air, and exposure to Te can result in the unpleasant condition known as "tellurium breath," whereby the victim's breath reeks of a garlic-like odor.

Similar to Bi films, behavior of Te films depends on the deposition rate, film thickness, and annealing conditions. In general, Te electrical conductivity increases with increasing thickness and deposition rate, and with inclusion of an anneal step [16-1718]. The higher conductivity is a result of larger crystal formation, which increases mobility. Mansingh and Garg found that the grain size of a 5000 Å thick Te film increased from 500 Å to 850 Å with a 425 K anneal under vacuum [18]. Conductivities for different conditions from several references are given in Table 3.2.

Tellurium has been suggested as a bolometer candidate since thin film Te has a high value of $\frac{dR}{dT}$ [19], and responsivities 100 times that of Bi have been reported [11]. Similar to Bi, Te has a negative temperature coefficient of resistivity.

Reference	Substrate type and temp (K)	deposition rate (A/min)	conductivity: pre/post anneal $(\Omega\text{-cm})^{-1}$	Anneal time and temp (K)
Dinno [17]	glass at 297 K	100	3.0 5.8	12 hr. at 423 K
Mansingh [18]	Si at 298 K	200	.15 .50	unknown time, 425 K
Mansingh [16]	glass at unknown Temp.	200	0.5 -	-
Wentworth [11]	glass at 298 K	240-300	3.7 -	-

Table 3.2: Comparison of selected thin film tellurium properties from a number of references.

3.3 Microbolometer Fabrication

The general fabrication of a conventional antenna-coupled microbolometer begins with formation of contact pads upon thoroughly cleaned substrates. The substrates used have either been glass, for establishing the process and obtaining dc characteristics, or fused quartz, which is transparent to far infrared radiation. Contact pad formation begins with e-beam evaporation of a thin layer of chromium, followed by a layer of gold. The Cr is deposited to provide good adhesion of the Au to the chip. This Cr/Au forms an electrically continuous base layer upon which Au may be electroplated. The contact pad areas are next defined by a routine photolithographic step (see appendix B). Gold is electroplated on these open areas to form 5-10 μm thick gold pads,which will facilitate wire-bonding after completion of device fabrication. The electroplating procedure is given in appendix C. Next, these gold pads are protected by photoresist as the undesired Cr/Au base layer is etched away. The gold was etched in Transene Gold Etchant Type TFA at room temperature for 45-60 seconds, and the Cr was then removed using Transene Chromium Mask Etchant at room temperature for typically 2 minutes. The chip is recleaned and is ready for antenna/microbolometer fabrication.

Metals for both the antenna and the microbolometer are deposited in a single vacuum deposition step. Such *in-situ* processing results in devices with minimal contact noise [10], but requires a special processing sequence. A photoresist bridge technique, and 3-pocket electron-beam evaporation, are discussed in the next two sections.

3.3.1 Photoresist Bridge/Liftoff Process

Metal patterning using wet and dry etching techniques first requires deposition of a metal layer, followed by photoresist application and pattern development, and finally an etch. Liftoff processing does away with the etch step, and makes photoresist bridge processes possible. In the liftoff process, the photoresist layer is applied and patterned before metal deposition. After photoresist patterning and development, metal is deposited and contacts the substrate only in the regions of developed photoresist. The unwanted metal, which sits atop the photoresist layer, is removed or 'lifted off' upon immersion in a photoresist solvent . Successful liftoff

requires a non-conformal coating of the metal; that is, the metal on the substrate must not be connected to the metal atop the masking layer. To insure the non-conformal coat, the mask material must have either a lip or a recessed wall, and the metal must be deposited in a directional manner, hence thermal evaporation is used rather than sputtering.

Normal positive photoresist processing results in at best a slightly sloped profile since the exposing source radiation attenuates as it travels through the resist. Special techniques are therefore required to create the overhang needed for liftoff. In one technique, an electron beam writes the desired pattern into a radiation sensitive resist such as polymethylmethacrylate (PMMA) [20]. The electron beam tends to scatter after it strikes the photoresist surface. This spreading of the beam as it descends results in negatively sloped resist sidewalls that are ideal for liftoff. This method has the capability of patterning submicron features and the PMMA can withstand higher processing temperatures than conventional photoresist. The major disadvantage of e-beam lithography is low throughput; writing a pattern in photoresist with an e-beam is very slow. This method was extensively studied in the '60s and early '70s [21].

A second technique involves modifying the surface of photoresist to slow down its development rate relative to the rest of the resist. The most successful way to do this is to soak the photoresist in chlorobenzene. This technique has been studied and optimized by IBM researchers [22-2324].

A third method is the liftoff process using edge detection (LOPED). This process, introduced by Pai and Oldham [25], is interesting because it does not require a lip for liftoff, and also does not require a directional metallization. It combines elements of traditional liftoff with wet etching.

The method used in this study is one of several multilayer photoresist techniques [26-2728]. Creation of the overhang structure is accomplished by stacking three layers. The bottom layer is fully exposed positive resist, and the top layer is positive resist that is patterned and developed normally. These two layers must be separated by a buffer layer to prevent intermixing, and to prevent removal of the bottom layer as the top is developed. After development of the top layer, the exposed buffer is removed. The developer now acts as an etchant, removing the

bottom layer until the desired undercut is reached. Besides the usual advantages associated with liftoff, this technique offers improved linewidth control over steps since the upper layer of resist is planarized by the lower layer.

The buffer layer is the critical component in this process. In the past, a thin layer of aluminum has been used. However, aluminum can create problems with alignment since it is opaque, and it also involves a lengthy vacuum deposition step [28]. An alternative method discovered by Hewlett-Packard researchers uses a plasma-formed buffer layer. The bottom layer of resist is subjected to a CF_4 plasma, which renders the surface inert, and prevents intermixing when the top layer is applied [[29]]. This fluorinized layer is insoluble in developer, and is somewhat insoluble in solvents such as acetone. The processing sequence is given in Fig. 3.4. The positive photoresist chosen for both layers is AZ 1350J. The bottom layer is spun on and pre-baked (at 75 °C), followed by a thorough flood exposure (Fig. 3.4a). A thin buffer layer is formed in a teflon chamber containing a CF_4 plasma (Fig. 3.4b). This layer is typically 300-400 Å thick, and ECSA spectra show all C-H bonds have been converted to C-F bonds [[30]]. The fluorinized layer is created by diffusion of free fluorine into the resist. An all-teflon plasmod chamber is therefore used because a glass chamber would consume most of this free fluorine. The fluorinized buffer layer has a low surface energy and will therefore not allow a top layer of photoresist to stick to it without further modification. The next step, then, is to slightly roughen the surface in an N_2 plasma to enhance adhesion of the second layer of photoresist. Although the mechanism is not understood, this N_2 plasma step has been found to replace some of the C-F bonds with C-H bonds, thus allowing the next layer of resist to stick [22]. Adhesion promoter is not used for this second layer since it has been found to occasionally damage the buffer layer. Otherwise the second layer of photoresist is processed routinely. After development of the top layer (Fig. 3.4c), the now-exposed portions of the buffer layer are removed by an oxygen plasma (Fig. 3.4d). Developer is now used as an etchant for the bottom layer, and a photoresist bridge is formed, as shown in Fig. 3.4e. The detailed lab procedure for the CF_4 plasma process is provided in appendix D.

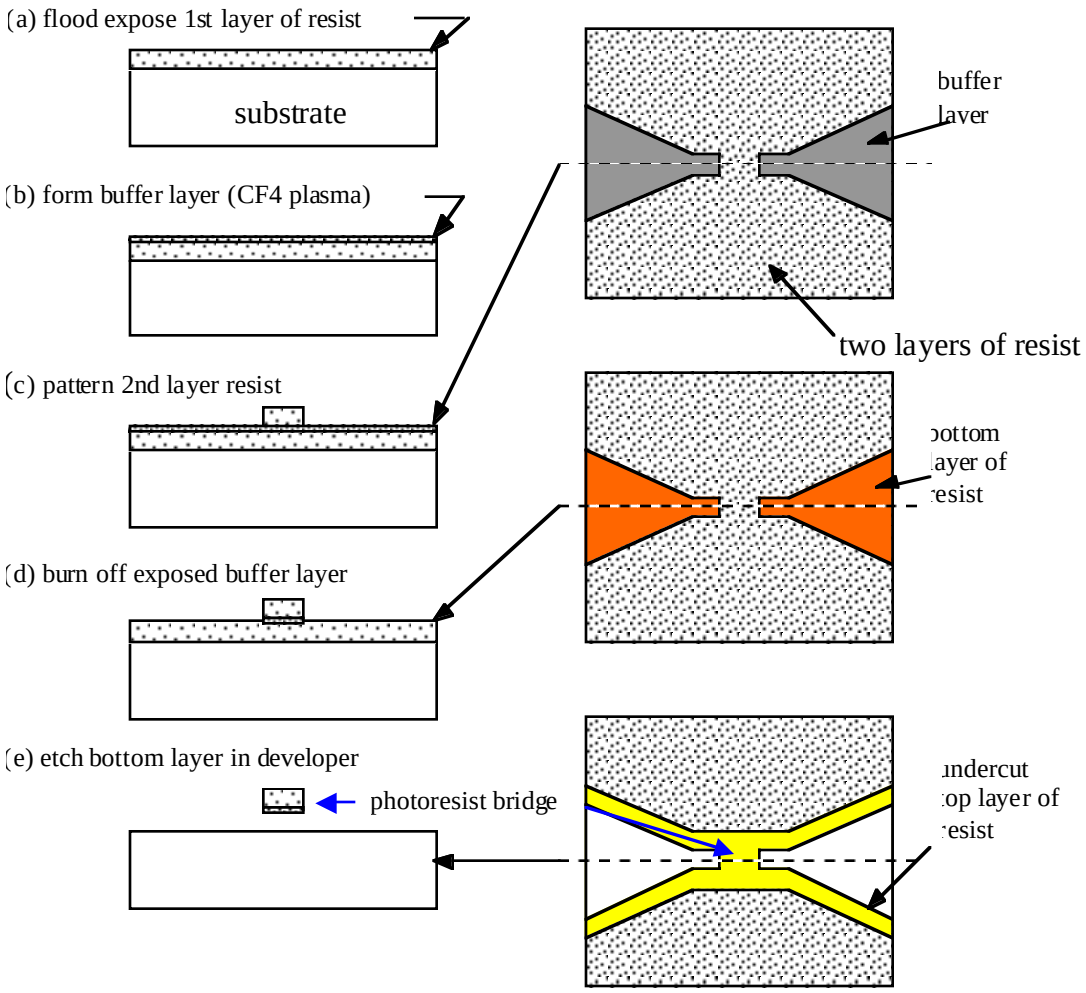

Fig. 3.4: The bilayer photoresist bridge process using a CF_4 generated buffer layer. (a) The first layer of photoresist is flood exposed. (b) A transparent buffer layer is formed by a CF_4 plasma, and roughened by an N_2 plasma to promote top layer adhesion. (c) The second layer photoresist is patterned. (d) The thin buffer layer is burned away by an O_2 plasma. (e) The bottom layer is etched in developer to form a bridge structure. Also formed is a well defined lip for lift-off metallization.

In the bridge process used to create microbolometer devices, metal for the antenna or signal line is evaporated at normal incidence to the substrate, and the narrow photoresist bridge casts a shadow in the detector region. The microbolometer material is then evaporated at an angle to the substrate such that deposition is accomplished under the photoresist bridge. The chip is soaked in acetone to lift off the unwanted metal. The top layer of photoresist forms a lip (Fig. 3.4e) which facilitates this liftoff step.

Figure 3.5 shows an SEM photograph of a photoresist bridge used in making microbolometers. Notice in this picture that the top layer of photoresist has a slightly positive slope to it (it is not recessed). The lip is therefore necessary for liftoff. Notice also the well-formed photoresist bridge, and the 'dimples' at either end of the bridge. These dimples are thought to arise from an interference effect in the second exposure step.

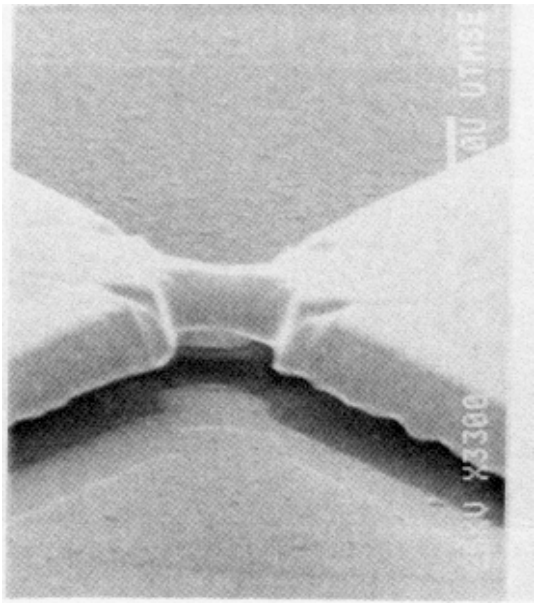

Fig. 3.5: SEM photograph of a photoresist bridge used for microbolometer fabrication.

3.3.2 Vacuum Deposition

Vacuum deposition took place in a system consisting in part of a mechanical roughing pump, a diffusion pump column, and a liquid nitrogen cold trap. This system is called "STUVAC" for identification purposes. The mechanical pump was a Leybold-Heraeus Trivac "A" Dual Stage Rotary Vane pump, and the diffusion pump was a D.P.D. Series DPD6-2400 rated at 2400 l/sec of air. Vacuum pressures of less than 10^{-6} torr were routinely achieved and maintained during evaporation. A procedure for using the STUVAC vacuum system is given in appendix E.

Successful fabrication of microbolometers using the photoresist bridge process requires two things: a tilting substrate holder, and a fixed evaporation point. The tilting substrate holder is necessary in order to evaporate metal beneath the photoresist bridge. The tilt plane should be located at or near the surface of the substrate. In addition, a scale is needed to enable repeatable settings at the same tilt angle. In STUVAC, a tilting substrate holder meeting these requirements was mounted on the top plate of the vacuum system. The fixed evaporation point is needed so that the photoresist bridge will always cast its shadow in the same places on the chip. This criterion was met by using a Thermionics three-pocket e-gun to evaporate all metals. For this electron beam evaporator, the 4 kV filament source and the magnet used to curve the beam over into the hearth were fixed in place, and the three hearths, or pockets, could be moved into position using a linear motion feedthrough.

In general, gold was always used as the antenna metal (following a Cr layer for adhesion). Silver was also used, but attempts to adhere Te to Ag failed miserably, resulting in a flaky, unreliable film.

3.4 Bismuth and Tellurium Microbolometers

Devices fabricated with Bi and Te were tested from 90 K to 320 K using an MMR low temperature microprobe station [11]. Both devices were fabricated on 33 mil thick fused quartz and consisted of a 1000 Å thick microbolometer adjoining a gold bow-tie antenna. For the antenna, 250 Å of Cr was used for adhesion followed by 1500 Å of gold. The detector material was then evaporated at 60°

angles at a rate of 6-8 Å/sec under vacuum maintained below 10^{-6} torr. All thicknesses were measured during evaporation with a crystal thickness monitor. Excess metal was lifted off using acetone as the photoresist solvent.

Figure 3.6 shows the dependence of resistance on ambient temperature for the two microbolometers. The slopes for both materials stay fairly constant throughout the temperature range measured. The electrical conductivities of the thin films are extracted from the experimental data using a two-dimensional finite difference thermal model of the microbolometer. As shown in Table 3.3, the α and σ obtained at 300 K for Bi is comparable to those given by Neikirk *et al.* [4]. Figure 3.7 shows the plots for the Te device operating at 300 K and 150 K. The calculated responsivities for Bi biased at 0.1 V and Te biased at 2 V are also listed in Table 3.3. The -2100 V/W responsivity for Te at 300 K is the highest reported value for a room temperature microbolometer detector. Te devices have a significantly higher responsivity than Bi ones, due to Te's much larger value of $\frac{dR}{dT}$. Although the Te looks promising because of its high responsivity, its

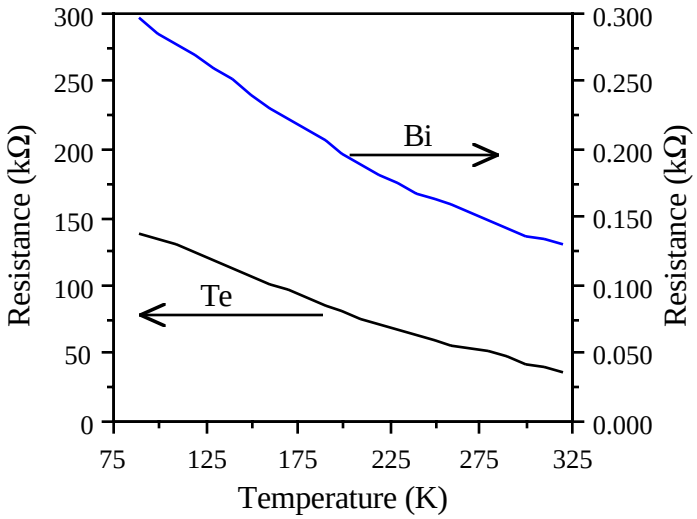

Fig 3.6: Resistance as a function of temperature for Te and Bi microbolometers.

	Bi 150 K	Bi 300 K	Bi [10] 300 K	Te 150 K	Te 300 K
length (μm)	6	6	4	5	5
width (μm)	4	4	3.5	3	3
R_b (Ω)	240	135	80	110×10^3	40×10^3
$\frac{dR}{dT}$ (Ω/K)	-.93	-.43	-.24	-560	-390
α (K^{-1})	-.0039	-.0032	-.003	-.0051	-.0098
σ $(\Omega\text{-cm})^{-1}$	620	1100	1460	1.4	3.7
V_b (V)	0.1	0.1	0.1	2.0	2.0
$\frac{dR}{dP}$ (Ω/μW)	-.095	-.028	-	-150	-42
$\mathbf{r}_{dc}$ (V/W)	-40	-21	-20	-2700	-2100

Table 3.3: Properties of Bi and Te microbolometers. $\mathbf{r}_{dc}$ is measured at the indicated bias voltage V_b.

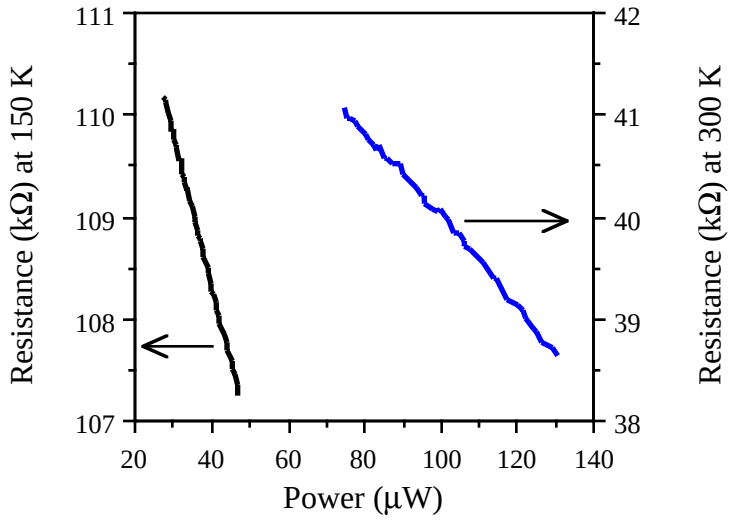

Fig. 3.7: Resistance as a function of dissipated power for the Te microbolometer at 150 K and 300 K biased at 2 V.

high resistance makes direct coupling to a planar antenna difficult. However, alternative composite structures for impedance matching could be developed to utilize such high resistance detectors. The combination of new antenna structures and high responsivity microbolometers may allow a significant improvement in far-infrared detector sensitivity.

3.5 Composite Microbolometers

As seen in the last section, the resistance of Te is too high to simply match with typical planar antenna impedances of 100-200 Ω. One solution to the mismatched load problem is to separate the load from the detector in a composite microbolometer structure, as shown in Fig. 3.8 [11]. The load, which is impedance-matched to the antenna, is in intimate thermal contact with, but is

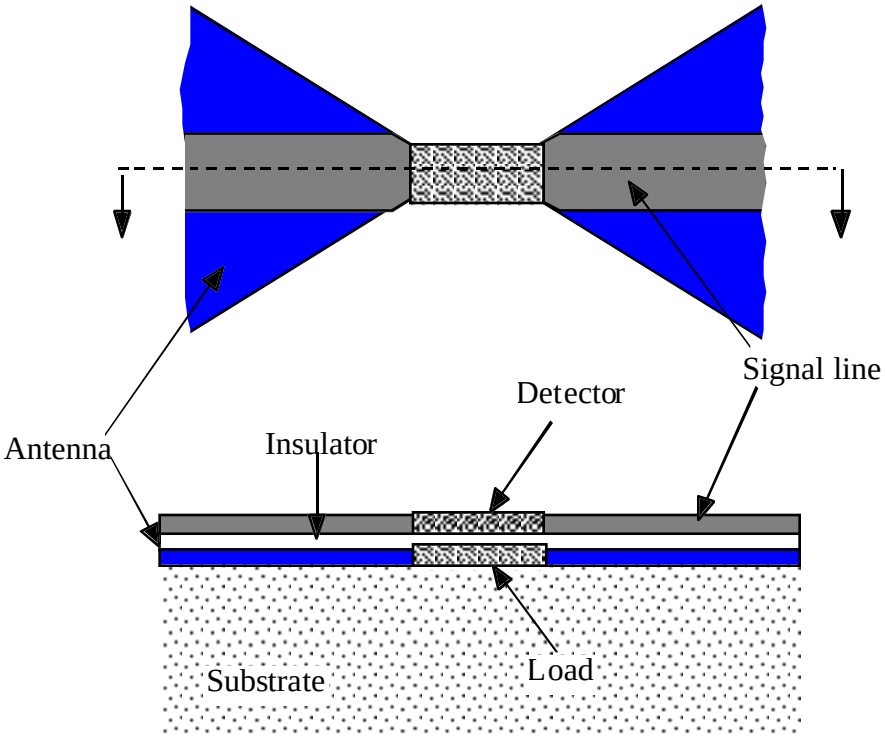

Fig. 3.8: Top view and cross section of a composite microbolometer. The load is impedance-matched to the bow-tie antenna, and is thermally coupled to a detector.

electrically isolated from, the detector element. Changes in load temperature will be quickly followed by changes in detector temperature, and hence by changes in detector resistance.

3.5.1 Theory

The composite microbolometer can be represented by the simple electrical circuit shown in Fig. 3.9, where the load and detector elements are shown physically close together. The dc responsivity in the Te detector $\mathbf{r}_d$ for a given amount of power W_d dissipated in the Te element can be written

$$\mathbf{r}_d = \frac{dV_d}{dW_d} = \frac{V_d}{R_d}\frac{dR_d}{dW_d} \qquad (3.1)$$

where V_d, I_d, and R_d are the voltage, current, and resistance, respectively, associated with the detector. Equation (3.1) is the general equation for a conventional microbolometer. This equation can be modified to determine the composite microbolometer responsivity $\mathbf{r}_{CB}$. The Te detector response to a change in power dissipated across the NiCr load element is

$$\mathbf{r}_{CB} = \frac{dV_d}{dW_d}\frac{dW_d}{dW_l} = \frac{V_d}{R_d}\frac{dR_d}{dW_l} \qquad (3.2)$$

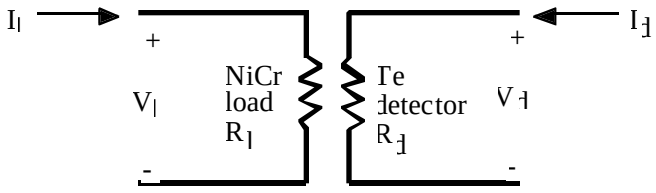

Fig. 3.9: A simple electrical circuit for the composite microbolometer.

where $\mathbf{r}_{CB}$ is the dc composite microbolometer responsivity, and the 'l' subscripts denote NiCr load properties. In (3.2) there is an efficiency term relating how much heat is dissipated in the detector for a given amount of heat dissipated in the load:

$$\eta_{th} = \frac{dW_d}{dW_l} = \frac{\mathbf{r}_{CB}}{\mathbf{r}_d} \qquad (3.3)$$

where η_{th} is the thermal coupling efficiency. This efficiency term depends on alignment of the top layer over the bottom layer, the separating insulator thickness, and the thermal properties of the separating layer. Since η_{th} is desired maximum, the separating insulating layer should be as thin as possible, with a high thermal conductivity.

3.5.2 Fabrication

Composite microbolometers have been fabricated consisting of nichrome as the load, Te as the detector, and SiO_x as the insulator. These devices were fabricated on a glass slide substrate upon which gold contact pads had been electroplated. Gold was also used for both the antenna leads and the signal line. Both device layers were produced using the photoresist bridge technique described in section 3.3.1.

Vacuum deposition was carried out at less than 10^{-6} torr, at deposition rates ranging from 2 Å/sec for NiCr to 10 Å/sec for Te and gold. The 80% Ni-20% Cr load was approximately 1500 Å thick, in contact with a 1500 Å thick gold bow-tie antenna. Following deposition of an 1800 Å thick SiO_x layer, the signal line/detector layer was fabricated. The Te detector was about 1200 Å thick, contacted to a 2000 Å thick gold signal line. The lengths and widths were about the same for both NiCr and Te elements, ranging from 4.5 to 5.0 μm.

The SiO_x layer was formed by plasma-enhanced chemical vapor deposition. The CVD was carried out under a 170 torr pressure of O_2 and 80 torr of silane. The O_2 was passed through rf coils to produce an oxygen plasma, then mixed with silane just above the chip surface. The substrate was held at 330°C, and deposition took place over 40 minutes. To measure the thickness of the deposited oxide, a

bare Si chip was placed next to the device chip during the CVD process. Thickness of the SiO_x layer on the bare Si chip was measured ellipsometrically. Contacts were opened through the SiO_x layer by a brief hydrofluoric acid etch.

The composite microbolometer is shown in the SEM photograph of Fig. 3.11. Notice the grainy appearance of the Te element. The nichrome element is not visible in this picture.

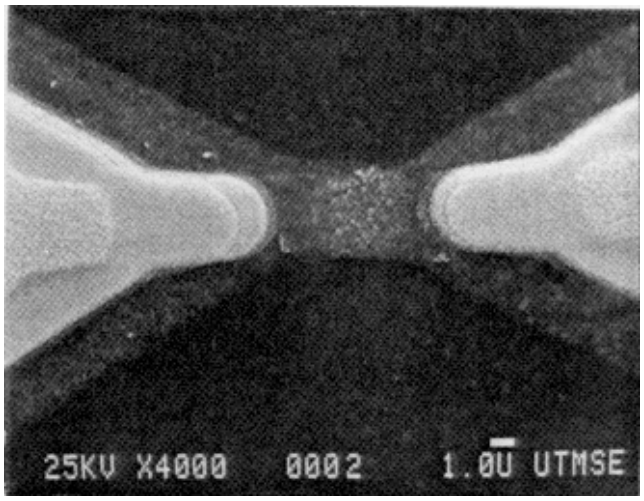

Fig. 3.10: SEM photograph of the composite microbolometer. The Te element is visible; the underlying NiCr load is not.

3.5.3 Measurement

Performance of the composite microbolometer depends on responsivity of the Te detector. Since this is a bolometer detector, resistance is a linear function of dissipated power. Thus, the dR_d/dW_d in (3.1) can be found from the slope of the Te detector resistance-power plot of Fig. 3.11. For a 0.75V bias, the Te detectors had a $\mathbf{r}_d$ of -510 V/W.

The detector resistance R_d can also be measured as a function of power dissipated in the nichrome load element. Figure 3.12 shows several such R_d-W_l plots at different Te detector bias voltages. Notice that the higher bias voltages result in lower resistance plots. The devices operate at a room temperature ambient, but the actual temperature in the vicinity of the Te element depends on its bias voltage, and on the heat transferred from the NiCr element. At higher V_d, the steady-state temperature of the Te element is higher. This results in lower overall resistance since thin film Te has a negative temperature coefficient of resistivity.

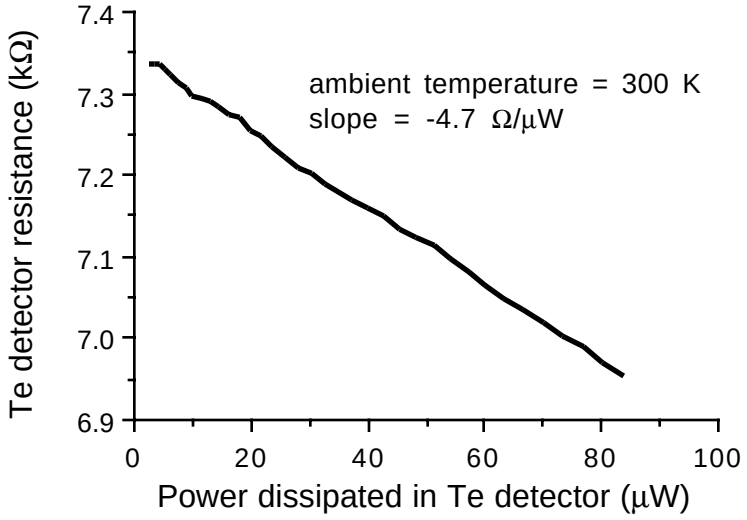

Fig. 3.11: The Te detector resistance is plotted versus power dissipated to determine dc responsivity of the free standing Te element.

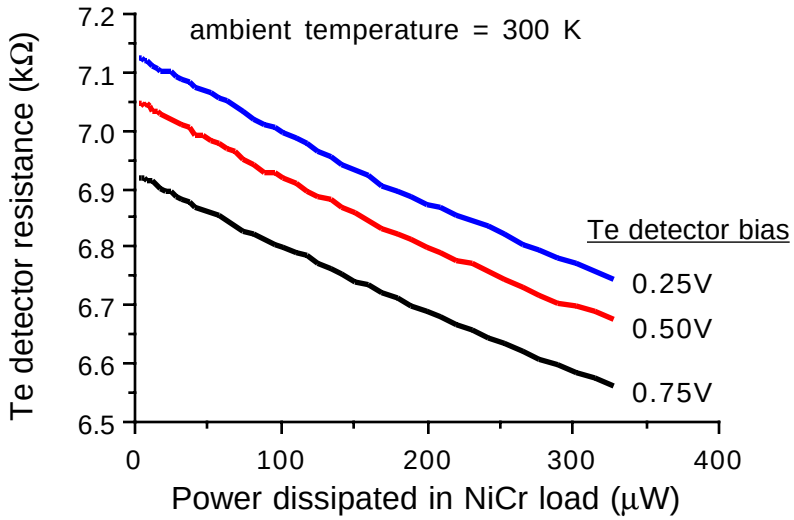

Fig. 3.12: The tellurium resistance is plotted versus power dissipated by the nichrome load element. For a particular bias voltage V_{bd} across the Te detector, the slope of the plot can be used to calculate dc responsivity.

The dc responsivity $\mathbf{r}_{CB}$ of a composite microbolometer can be found by taking the slope of the resistance-power plot, just as was done for the conventional microbolometer. From Fig. 3.12, the slope dR_d/dW_l at V_{bd} = 0.75V leads to a responsivity $\mathbf{r}_{CB}$ = -120 V/W. From this result and the result found for $\mathbf{r}_d$, the thermal coupling efficiency is calculated as η_{th} = 0.24.

Figure 3.13 illustrates the general measurement setup for measuring speed of response. Two 220 MHz rf sources are beat together at an adjustable frequency, and fed through a high pass filter to the antenna leads. The NiCr element changes temperature in response to the modulation frequency, and this temperature change is felt by the Te detector. A bias network consisting of a 6V battery and resistors supplies a steady bias across the Te detector. The signal drawn off the detector is fed through a low pass filter and monitored by an oscilloscope for beat frequencies ranging from 100 Hz to 200 kHz. The responsivity of the device is the ratio of this signal voltage to the power dissipated in the load element. This dissipated power is

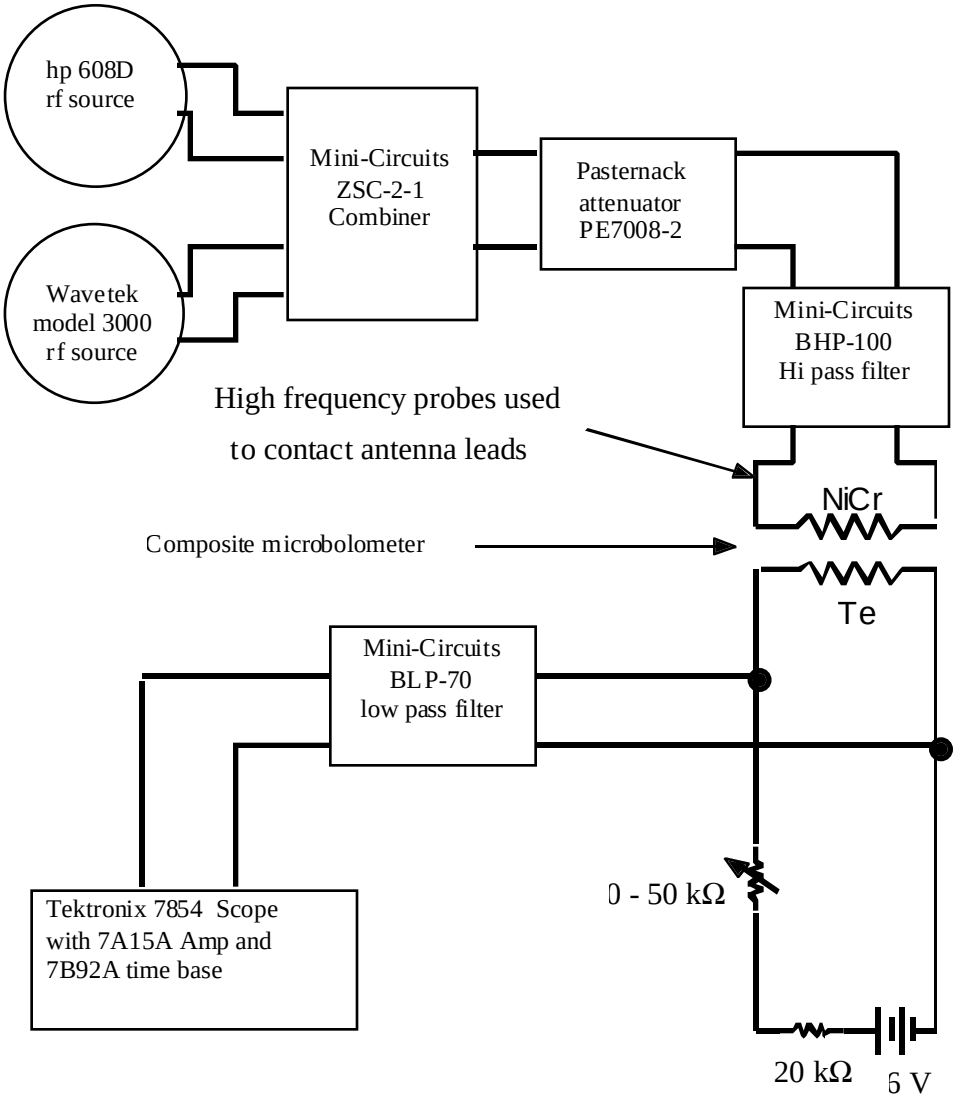

Fig. 3.13: rf measurement setup for the composite microbolometer.

difficult to measure directly. However, at low frequencies the responsivity approaches the dc responsivity. Therefore, since dc responsivities have been determined, the power dissipated in the NiCr load element can be estimated. This dissipated power is assumed constant over the frequency range tested. The signal voltages are then divided by this dissipated power term to obtain responsivity as a function of frequency.

Figure 3.14 shows the responsivity curve generated for the composite microbolometer at a Te detector bias of 0.75V. This figure also shows the noise voltage measured across the Te detector element at the same voltage. The noise is measured with a PAR 124A lock-in amplifier with 117 preamp over a bandwidth of 10% of the selected center frequency. Since the Johnson noise floor is about 10^{-8} V/$\sqrt{\text{Hz}}$, it is clear from this figure that a 1/f-type noise is dominant. The NEP plot in Fig. 3.15 is calculated by dividing the noise by the responsivity. The device has a minimum NEP of 6.7 x 10^{-9} W/$\sqrt{\text{Hz}}$ at 30 kHz. For comparison, a Bi microbolometer typically has an $\mathbf{r}_{dc}$ of 20 V/W, and minimum NEP of 10^{-10} W/$\sqrt{\text{Hz}}$ at 10 kHz.

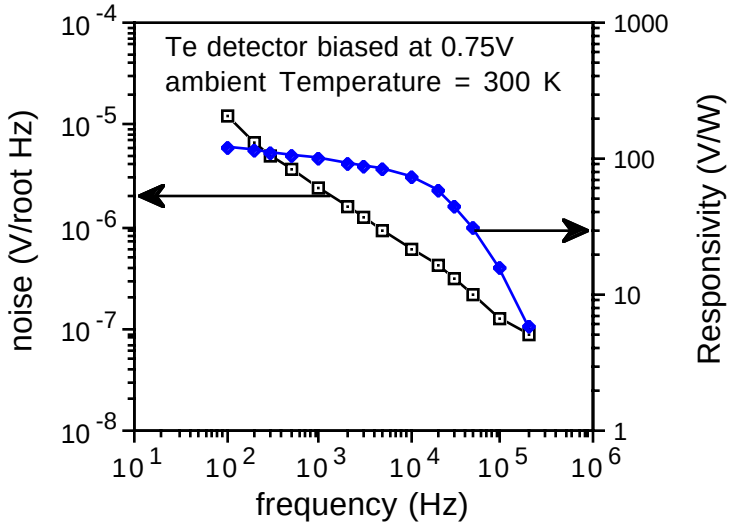

Fig. 3.14: Noise and responsivity are plotted versus beat frequency for a composite microbolometer with the Te detector element biased at 0.75V.

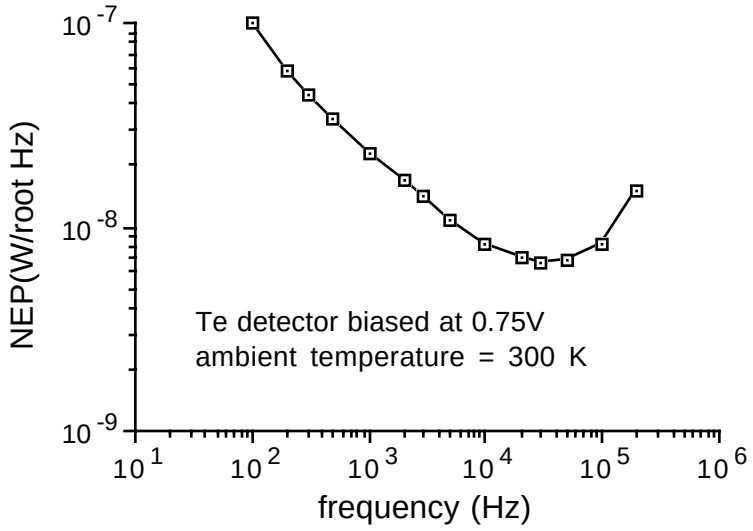

Fig. 3.15: Sensitivity for the composite microbolometer versus beat frequency, with the Te detector element biased at 0.75V. Best performance occurs at about 30 kHz, where NEP = 6.7 x 10^{-9} W/$\sqrt{\text{Hz}}$.

3.5.4 Thermal Model

A thermal model for the composite microbolometer is useful for better understanding of device operation, and for guiding the design of an optimized structure. The method is generally the same as that described in section 2.4. In this section, details for a composite microbolometer structure are given.

A two dimensional cross section of the device is shown in Fig. 3.16. As before, symmetry allows for treatment of only half of the device. The model is simplified by considering the antenna and signal lines to be perfect conductors, and the antenna/load and signal line/detector layers each occupy only one layer. The substrate and separating insulator layers are also assumed to have infinite electrical resistance.

The composite microbolometer model must consider heat generation terms for both the NiCr load elements and the Te detector elements. For the detector elements

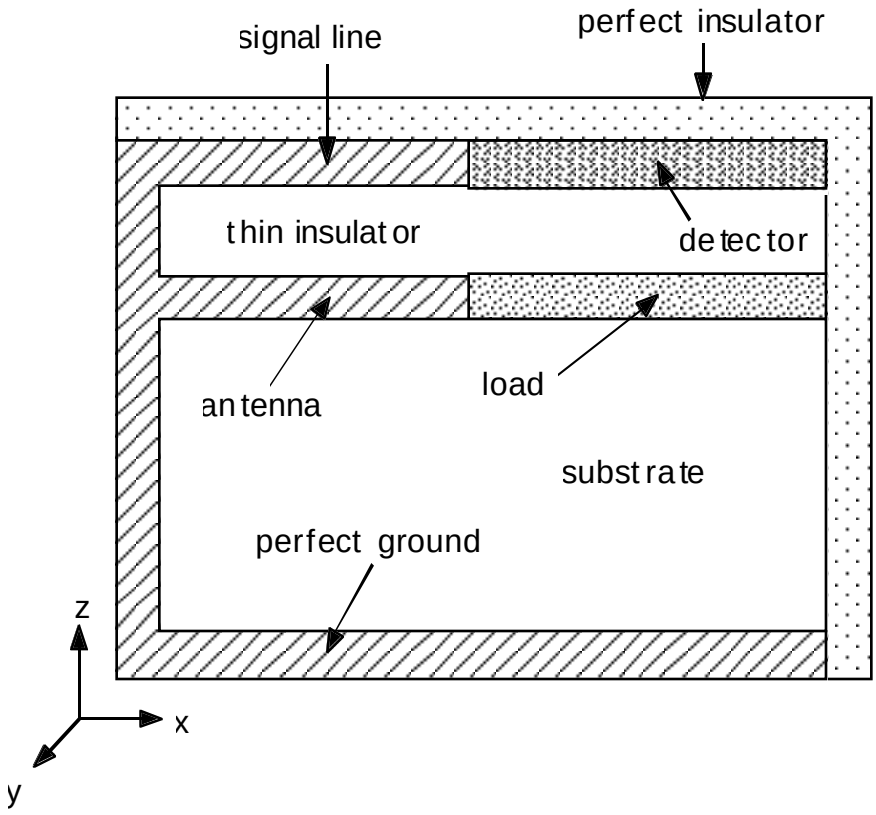

Fig. 3.16: The composite microbolometer thermal model profile.

$$q_i = I_d^2 R_i \qquad (3.4a)$$

and for the load elements

$$q_i = I_l^2 R_i \, . \qquad (3.4b)$$

I_d and I_l are the currents through the elements, and R_i is the element resistance. For the NiCr load elements, resistance is fairly constant with temperature. For the Te detector elements, resistance depends on temperature by

$$R_i = R_{io} + \frac{\Delta R_d}{\Delta T} \Delta T_o \qquad (3.5)$$

where R_{io} is the ambient temperature, $\Delta R_d/\Delta T$ is the detector temperature coefficient, and ΔT_o is the temperature deviation from ambient.

The iterative procedure detailed in chapter 2 is again used to generate an isothermal plot, shown in Fig. 3.17. The material parameters in the thermal model may be adjusted to give dc responsivities which match both the composite microbolometer and the Te element by itself. These parameters are listed with Fig. 3.17.

3.5.5 Conclusions

A composite microbolometer has been demonstrated which utilizes a NiCr load element thermally coupled to a Te detector. The sensitivity and speed of these devices have been measured, and these results are being used to formulate a thermal model for aid in designing an optimum composite structure. Although a conventional Bi microbolometer has a reasonable NEP, its low responsivity makes detection of low power levels difficult. The higher responsivity of these composite structures may make it easier to detect these low levels, and could therefore ease amplification requirements in receiver systems.

The sensitivity of the composite microbolometers could probably be improved by using thinner Te detectors with higher responsivity. Another way to increase device responsivity is to use a thinner separating layer between the load element and the detector, or by using a high thermal conductance material, such as diamond thin film, for the separating layer. Finally, sensitivity can be improved by decreasing 1/f noise in the Te detectors.

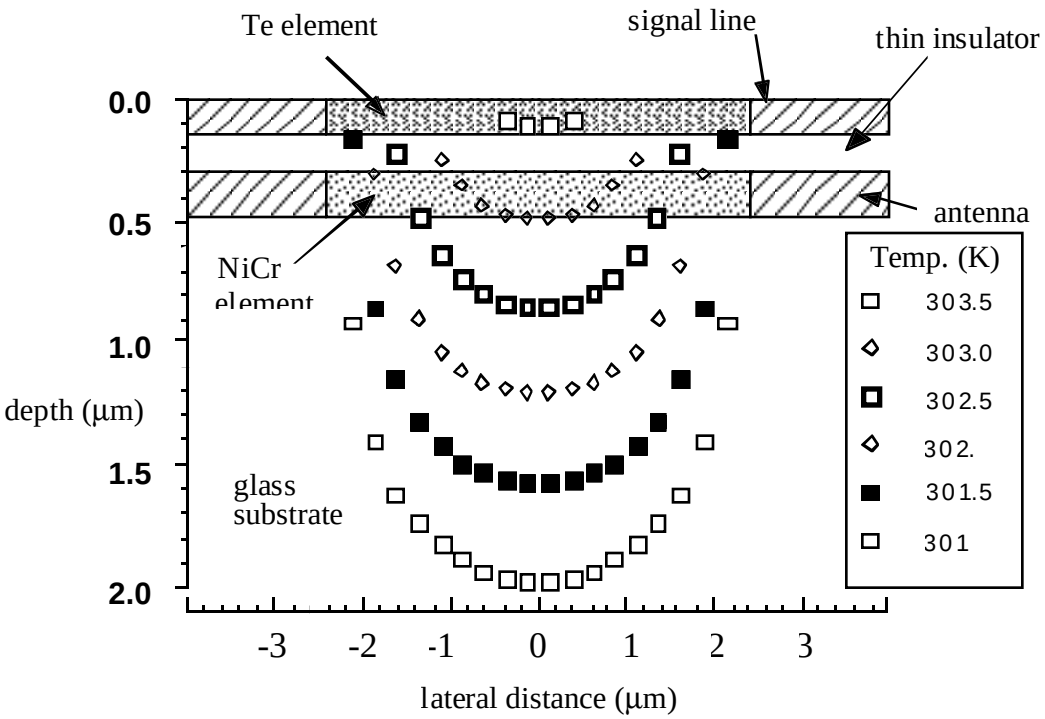

Fig. 3.17: Isotherms for the composite microbolometer with the following properties:

	Te	NiCr	SiO_x	glass
k(W/cm-K)	.24	.125	.0013	.014
σ(Ω-cm)-1	10.9	350	-	-

The figure is stretched in the depth direction relative to the lateral direction.

References:

[1]. N.W. Ashcroft and N.D. Mermin, Solid State Physics, 1st Ed., Holt, Rinehart and Winston, p. 127, 1976.

[2]. S. Kochowski and A. Opilski, "Concentration and Mobility of Charge Carriers in Thin Polycrystalline Films of Bismuth," *Thin Solid Films*, Vol. 48, pp. 345-351, 1978.

[3]. S. Baba, K. Sugawara, and A. Kinbara, "Electrical Resistivity of Thin Bismuth Films," *Thin Solid Films*, Vol. 31 , pp. 329-335, 1976.

[4]. F. Völklein and E. Kessler, "Analysis of the Lattice Thermal Conductivity of Thin Films by Means of a Modified Mayadas-Shatzkes Model: The Case of Bismuth Films," *Thin Solid Films*, Vol. 142, pp. 169-181, 1986.

[5]. A. Kawazu, Y. Saito, H. Asahi, and G. Tominaga, "Structure and Electrical Properties of Thin Bismuth Films," *Thin Solid Films*, Vol. 37, pp. 261-266, 1976.

[6]. A.V. Joglekar, R. N. Karekar, and K. Sathianandan, "Electrical resistivity of polycrystalline bismuth films," *J. Vac. Sci. Technol.*, Vol. 11, No. 2, pp. 528-529, Mar./Apr. 1974.

[7]. S. Chaudhuri and A. K. Pal, "*In situ* measurement of Hall effect, magnetoresistance, resistivity, and TCR of bismuth films," *J. Appl. Phys.*, Vol. 48, No. 8, pp. 3455-3461, Aug. 1977.

[8]. L. K. J. Vandamme and J. Kedzia, "Concentration, Mobility and 1/f Noise of Electrons and Holes in Thin Bismuth Films," *Thin Solid Films*, Vol. 65, pp. 283-292, 1980.

[9]. A.H. De Kuijper and J. Bisschop, "Temperature Dependence of Concentrations and Mobilities in Thin Bismuth Films," *Thin Solid Films*, Vol. 110, pp. 99-106, 1983.

[10]. D.P. Neikirk, "Integrated detector arrays for high resolution far-infrared imaging," Ph.D. thesis, California Inst. of Technol., 1984.

[11]. S.M. Wentworth and D.P. Neikirk, "Far Infrared Microbolometers Made with Tellurium and Bismuth," *Electronics Letters*, Vol. 25, No. 23, pp. 1558-1560, 9 Nov. 1989.

[12]. S. Kochowski, "An anomalous dependence of the specific resistance on thickness for thin films of Bi in the temperature range 78 - 293 K," *Thin Solid Films*, Vol. 28, pp. L35-L37, 1975.

[13]. Y. Yasuoka, H. Hirayama, and T. Miyata, "Tellurium Thin-Film Field-Effect Transistor Deposited on TGS Crystal," *Jpn. J. Appl. Phys.*, Vol. 16, No. 7, pp. 1195-1201, July 1977.

[14]. H.L. Wilson, W.A. Gutierrez, "Tellurium TFT's Exceed 100-MHz and One-Watt Capabilities," *Proc. IEEE*, 55, pp. 415-416, 1967.

[15]. J. Grosvalet and C. Jund, "Influence of Illumination on MIS Capacitances in the Strong Inversion Region," *IEEE Trans. Electron Devices*, Vol. ED-14, No. 11, pp. 777-780, Nov. 1967.

[16]. A. Mansingh and A.K. Garg, "Hopping Transport in Evaporated Polycrystalline Tellurium Films," *Thin Solid Films*, Vol. 131, pp. 41-50, 1985.

[17]. M.A. Dinno and M. Schwartz, "Structural dependence of electrical conductivity of thin tellurium films," *J. Appl. Phys.*, Vol. 45, No. 8, pp. 3328-3331, Aug. 1974.

[18]. A. Mansingh and A.K. Garg, "Electrical properties of (*p*)Te-(*p*)Si isotype heterojunction," *J. Appl. Phys.*, Vol. 56, No. 8, pp. 2315-2322, Oct. 1984.

[19]. B.H. Billings, W.L. Hyde, and E.E. Barr, "An Investigation of the Properties of Evaporated Metal Bolometers," *J. Opt. Soc. Am.*, Vol. 37, pp. 123-132, 1947.

[20]. D.A. McGillis, "Lithography," in VLSI Technology, S.M. Sze, ed., McGraw-Hill, pp. 281-287, 1983.

[21]. M. Hatzakis, "Electron Resists for Microcircuit and Mask Production," *J. Electrochem. Soc.*, Vol. 116, pp. 1033-1037, 1969.

[22]. M. Hatzakis, B. J. Canavello, and J. M. Shaw, "Single-Step Optical Lift-Off Process," *IBM J. Res. Develop.*, Vol. 24, No. 4, pp. 452-460, July 1980.

[23]. R. M. Halverson, M. W. MacIntyre, and W. T. Motsiff, "The Mechanism of Single-Step Liftoff with Chlorobenzene in a Diazo-Type Resist," *IBM J. Res. Devel.*, Vol. 26, No. 5, pp. 590-595, Sept. 1982.

[24]. G. G. Collins and C. W. Halsted, "Process Control of the Chlorobenzene Single-Step Liftoff Process with a Diazo-Type Resist," *IBM J. Res. Develop.*, Vol. 26, No. 5, pp. 596-604, Sept. 1982.

[25]. P. L. Pai and W. G. Oldham, "A Liftoff Process Using Edge Detection (LOPED)," *IEEE Trans. Semicond. Mfg.*, Vol. 1, No. 1, pp.3-9, Feb 1988.

[26]. Y. Homma, A. Yajima, and S. Harada, "Feature Size Limit of Liftoff Metallization Technology," *IEEE Trans. Electron Devices*, Vol. ED-29, No. 4, pp. 512-517, April 1982.

[27]. S. P. Lyman, J. L. Jackel, and P. L. Liu, "Lift-off of thick metal layers using multilayer resist," *J. Vac. Sci. Technol.*, Vol. 19, No. 4, pp. 1325-1328, Nov./Dec. 1981.

[28]. K. Grebe, I. Ames, and A. Ginzberg, "Masking of Deposited Thin Films by Means of an Aluminum-Photoresist Composite," *J. Vac. Sci. Technol.*, Vol. 11, pp. 458, Jan/Feb 1974.

[29]. C. Li and J. Richards, "A High Resolution Double Layer Photoresist Structure for Lift-Off Technology," *International Electron Devices Meeting*, Washington, DC, pp. 412-414, Dec. 8-10, 1980.

[30]. D. M. Dobkin and B. D. Cantos, "Plasma Formation of Buffer Layers for Multilayer Resist Structures," *IEEE Electron Device Lett.*, Vol. EDL-2,No. 9, pp. 222-224, Sept. 1981.